



1 Intraseasonal variability of the South Vietnam Upwelling, South  
2 China Sea: influence of atmospheric forcing and ocean intrinsic  
3 variability.

4

5 Marine Herrmann<sup>1\*</sup>, Thai To Duy<sup>2</sup>, Claude Estournel<sup>1</sup>

6 <sup>1</sup> Université de Toulouse, LEGOS (IRD/CNES/CNRS/UPS), Toulouse, France, 31400 Toulouse, France

7 <sup>2</sup> Institute of Oceanography (IO), Vietnam Academy of Science and Technology (VAST), Nha Trang, Vietnam

8 *Correspondence to* : Marine Herrmann (marine.herrmann@ird.fr)

9 **Short summary**

10 The South Vietnam Upwelling develops in summer along and off the Vietnamese coast. It brings cold and nutrient-  
11 rich waters to the surface, allowing photosynthesis essential to marine ecosystems and fishing resources. We show  
12 here that its daily variations are mainly due to the wind, thus predictable, in the southern shelf and coast regions.  
13 However, they are more chaotic in the offshore area, and especially in the northern area, due to the influence of  
14 eddies of a highly chaotic nature.



15                   **Abstract**

16   The South Vietnam Upwelling (SVU) develops off the Vietnamese coast (South China Sea) during the southwest  
17   summer monsoon over four main areas: the northern coastal upwelling (NCU), the southern coastal upwelling  
18   (SCU), the offshore upwelling (OFU) and the shelf off the Mekong River mouth (MKU). An ensemble of ten  
19   simulations with perturbed initial conditions were run with the fine-resolution SYMPHONIE model (1 km  
20   inshore) to investigate the daily to intraseasonal variability of the SVU and the influence of the ocean intrinsic  
21   variability (OIV) during the strong SVU of summer 2018.

22   The intraseasonal variability is similar for SCU, MKU and OFU, driven to the first order by the wind variability.  
23   MKU and SCU are induced by stable ocean dynamics (the northeastward then eastward boundary current) and  
24   have very little chaotic variability. The OIV has a stronger influence on OFU. In July, OFU mainly develops along  
25   the northern flank of the eastward jet. The influence of OIV is strongest and related to the chaotic variability of  
26   the meridional position of the jet. In August this position is stable and OFU develops mainly in the area of positive  
27   wind curl and cyclonic eddies north of the jet. The influence of OIV, weaker than in July, is related to the  
28   organization of this mesoscale circulation. NCU shows a completely different behavior from the other areas. In  
29   the heart of summer, the large-scale circulation formed by the eastward jet and eddy dipole is well established  
30   with an alongshore current preventing NCU. In early and late summer, the large-scale circulation is weaker,  
31   allowing a mesoscale circulation of strongly chaotic nature to develop in the NCU area. During those periods, the  
32   OIV influence on NCU is very strong and related to the organization of this mesoscale circulation: NCU is favored  
33   (annihilated) by offshore-oriented (alongshore) structures.

34

35                   **1. Introduction**

36   The summer general circulation in the central South China sea is largely induced by the prevailing southwest  
37   monsoon winds over the region (Wang et al., 2004; Wyrski et al., 1961). It is characterized by the development  
38   off the central Vietnamese coast of an anticyclonic gyre (AC) in the south and a cyclonic gyre (C) in the north  
39   (forming an eddy dipole referred to as the ACC dipole) and of the South Vietnamese upwelling, hereafter referred  
40   to as the SVU, that develops over four main areas. First, the convergence of two gyres creates an eastward jet  
41   departing from the southern part of the central coast of Vietnam between 11°N and 12°N. This convergence gives  
42   rise to an Ekman current-induced coastal upwelling (Dippner et al., 2007; Chen et al., 2012), hereafter referred to  
43   as SCU. Second, Ekman pumping-induced upwelling (OFU hereafter) develops offshore in the area of strong  
44   positive wind and surface current vorticity (Liu et al., 2012; Da et al., 2019; Ngo and Hsin, 2021). Third, recent  
45   studies have revealed that coastal upwelling (NCU hereafter) can develop along the northern part of the central  
46   Vietnamese coast (Da et al., 2019; Ngo and Hsin, 2021; To Duy et al., 2022). Last, To Duy et al. (2022) showed  
47   for the first time that upwelling develops off the Mekong Delta in the wake of Con Dao islands (see Fig. 1b, MKU  
48   hereafter). SVU participates to the nutrient enrichment of the surface layer, hence plays an important role in the  
49   biological productivity and in the halieutic resources of the region (Bombar et al., 2010; Liu et al., 2012; Loick-  
50   Wilde et al., 2017; Lu et al., 2018; Loisel et al., 2017). Some authors also showed that the SVU may influence the  
51   functioning of local and regional climate (Xie et al., 2003; Zheng et al., 2016). Understanding precisely the  
52   functioning and variability of the SVU and its response to long-term changes is therefore an important issue.



53 The interannual variability of the SVU has been investigated in numerous previous studies. In the SCU, OFU and  
54 MKU regions, the interannual variability of summer wind intensity is related to and in phase with the intensity of  
55 the summer monsoon, and is the main driver of the interannual variability of upwelling intensity (Wang et al.,  
56 2006; Chen et al., 2014; Li et al., 2014; Da et al., 2019; Ngo and Hsin, 2021; To Duy et al., 2022). ENSO (El Niño  
57 Southern Oscillation) also impacts the upwelling in those regions, due to its influence on summer monsoon wind  
58 (Wang et al., 2006; Kuo et al., 2004; Loick-Wilde et al., 2017; Da et al., 2019). Some studies (Li et al., 2014; Da  
59 et al., 2019) then revealed that ocean intrinsic variability (OIV) influences the interannual variability of the  
60 eastward jet and of the OFU. This influence of OIV is related to the spatial distribution of summer averaged  
61 surface current vorticity associated with eddies: cyclonic (anticyclonic) eddies located in the area of positive wind  
62 stress curl enhance (weaken) the Ekman pumping-induced OFU. The interannual variability of NCU shows a  
63 completely different behavior. Ngo and Hsin (2021) and To Duy et al. (2022) concluded that wind conditions  
64 favorable to SCU, MKU and OFU were unfavorable to NCU, and vice versa. To Duy et al. (2022) moreover  
65 showed that the influence of wind is weaker for NCU than for the other areas, and that the influence of circulation,  
66 in particular of the spatial organization of the strongly chaotic submesoscale to mesoscale circulation that prevails  
67 over the area, is stronger: on a seasonal average, NCU is inhibited when alongshore currents prevail, and enhanced  
68 when offshore circulation prevails.

69 The daily to intraseasonal variability of the SVU was much less studied. Available studies, all based on satellite  
70 data, focused on the SCU and OFU. Xie et al. (2007) showed that the upwelling in those areas does not develop  
71 smoothly during the summer, but shows a strong intraseasonal variability related to the wind variability and  
72 Madden Julian Oscillation (MJO). They suggested that SVU experiences two to four events of development and  
73 decay during the summer, in response to the wind fluctuations. Isoguchi and Kawamura (2006) and Liu et al.  
74 (2012) confirmed respectively for the period 2000-2002 and for summer 2007 that the MJO is a strong driver of  
75 the events of southwesterly wind intensification within the season and of the resulting upwelling. They moreover  
76 revealed the effect of tropical storms that can reinforce the southwesterly wind hence the SVU.

77 To better understand the functioning and variability of the SVU, it is therefore necessary to investigate in detail  
78 the functioning of its daily to intraseasonal variability over its four areas of development (SCU, NCU, OFU and  
79 MKU) and to identify the driving factors. Previous studies mentioned above revealed the role of wind for SCU  
80 and OFU, which should be examined for the other areas. The role of OIV in the interannual variability of the  
81 upwelling, related to mesoscale circulation and eddies in the coastal and offshore area, was highlighted for OFU  
82 and suggested for NCU. It should be examined at the intraseasonal scale, and requires an ensemblist approach as  
83 used by Waldman et al. (2017a, 2018). Chen et al. (2012) also showed from idealized simulations that tides and  
84 river plumes could be also involved in SVU variability, however, to our knowledge, only very few models used  
85 for the SVU study included the effect of tides, and none of them investigated their impact.

86 The present paper focuses on the daily to intraseasonal variability of the SVU over its four areas of development,  
87 examining in particular the role of atmospheric forcing (wind) and of ocean dynamics and its intrinsic variability.  
88 The effect of tides and rivers will be examined in a future study. A fine-resolution realistic model including tides  
89 and already presented and evaluated in To Duy et al. (2022) for the period 2009-2018 is used. Ensemble  
90 simulations with perturbed initial conditions are performed to study the case of summer 2018, which was an  
91 exceptionally strong summer of upwelling for SCU, OFU and MKU (Ngo and Hsin, 2021; To Duy et al., 2022).



92 The fine-resolution model and ensemble simulations and the definition of study areas, upwelling indicators and  
93 OIV indicators are presented in Part 2. The intraseasonal variability of the oceanic circulation and of the SVU,  
94 including the role of OIV, are examined respectively in Part 3 and Part 4. Results are summarized and future work  
95 is discussed in Part 5.

96

## 97 **2. Methodology**

### 98 **a) The 3D hydrodynamical ocean model SYMPHONIE**

99 To Duy et al. (2022) built a fine-resolution configuration of the 3-D ocean circulation model SYMPHONIE  
100 (Marsaleix et al., 2008, 2019) over the Vietnam coastal region (VNC hereafter), based on a horizontal polar grid  
101 with a resolution decreasing linearly seaward, from 1 km at the Vietnamese coast to 4.5 km offshore, and with 50  
102 vertical levels. We use exactly the same configuration here and show VNC domain in Figure 1a,b. The  
103 atmospheric forcing is computed from the 3-hourly output of the European Center for Medium-Range Weather  
104 Forecasts (ECMWF) 1/8° atmospheric analysis, distributed on <http://www.ecmwf.int>. Initial and lateral ocean  
105 boundary conditions are prescribed from the daily outputs of the global ocean 1/12° analysis PSY4QV3R1  
106 distributed by the Copernicus Marine and Environment Monitoring Service (CMEMS) on  
107 <http://marine.copernicus.eu>. The implementation of tides follows Pairaud et al. (2008, 2010) and considers the 9  
108 main tidal harmonics, provided by the 2014 release of the FES global tidal model (Lyard et al., 2006). Freshwater  
109 discharge is provided for 36 river mouths. More details about the model, its configuration and the forcings are  
110 provided in To Duy et al. (2022). They performed and evaluated a 10-year simulation over the period 2009-2018,  
111 hereafter called LONG, showing that it reproduces realistically the temporal (seasonal to interannual) and spatial  
112 variability of the SCS ocean dynamics and water masses. In the LONG simulation, a very strong SVU developed  
113 during summer 2018, due in particular to strong July-August wind (To Duy et al., 2022).

### 114 **b) The ensemble**

115 We performed an ensemble of ten simulations with perturbed initial conditions between January 1st, 2017 and  
116 December 31st, 2018. For that we used ten different initial conditions for temperature, salinity, sea surface  
117 elevation and currents fields. Most of the OIV develops at mesoscale (Serazin et al., 2015, Waldman et al., 2018),  
118 we therefore only perturbed the mesoscale field, following the same methodology as Waldman et al. (2017a,  
119 2017b, 2018): for the ten simulations of the ensemble, the large-scale state of the initial field is identical, and the  
120 small-scale of the initial field state differs. The common large-scale state is equal to the large-scale state of January  
121 1st, 2017 of the LONG simulation, computed using a 100 km low-pass filter. For XX going from 09 to 18, the  
122 small-scale state of January 1<sup>st</sup>, 20XX of the LONG simulation is computed using a 100 km high-pass filter. The  
123 initial state of member XX of the simulation ensemble is then computed by adding this small-scale state to the  
124 common large-scale state.

### 125 **c) Definition of upwelling areas**

126 Figure 1c,d shows the SST averaged over June-September (JJAS) 2018 for the ensemble average and for OSTIA  
127 (Operational Sea Surface Temperature and Sea Ice Analysis) reanalysis outputs, available at  
128 <ftp://data.nodc.noaa.gov/pub/data.nodc/ghrsst/L4/GLOB/UKMO/OSTIA/>. Simulated SST is in good agreement



129 with observations, showing a large area of colder surface water corresponding to the strong SVU that developed  
130 during summer 2018. We show in Figure 1b,c,d the four boxes used by To Duy et al. (2022), that correspond to  
131 the four main areas of SVU development: boxSC and boxNC for respectively the southern (SCU) and northern  
132 (NCU) coastal upwelling, boxOF for the offshore upwelling (OFU), and boxMK for the upwelling offshore the  
133 Mekong delta (MKU).

#### 134 **d) Indicators of upwelling intensity**

135 We compute a SST-based upwelling index following exactly the same methodology as Da et al. (2019) and To  
136 Duy et al. (2022). The daily upwelling index  $UI_d$  is computed at each point of the study area that verifies  
137  $SST(x,y,t) < T_o$  as:

$$138 \quad UI_d(x, y, t) = T_{ref} - SST(x, y, t) \text{ for } (x,y,t) \text{ where } SST(x,y,t) < T_o \quad (1)$$

139 The reference temperature  $T_{ref} = 29.2^\circ\text{C}$  is computed as the SST averaged over JJAS and over box $T_{ref}$ , the area  
140 east of the upwelling region that is the least impacted by upwelling (see Figure 1c,d), in the LONG simulation.  
141 The threshold temperature under which upwelling occurs,  $T_o = 27.6^\circ\text{C}$ , is defined as the optimal upwelling  
142 threshold that covers the largest number of upwelling occurrences but avoids to include cold water horizontally  
143 advected between upwelling areas.

144 For each box  $boxN$ , the daily upwelling index  $UI_{d,boxN}$  is computed as:

$$145 \quad UI_{d,boxN}(t) = \frac{\iint_{(x,y) \text{ in } boxN \text{ so that } SST(x,y,t) < T_o} (T_{ref} - SST(x,y,t)) \cdot dx \cdot dy}{A_{boxN}} \quad (2)$$

146 where  $A_{boxN}$  is the size of  $boxN$ . The yearly upwelling index  $UI_{y,boxN}$  is computed over the JJAS as:

$$147 \quad UI_{y,boxN} = \frac{\int_{JJAS} UI_{d,boxN}(t) dt}{ND_{JJAS}} \quad (3)$$

148 where  $ND_{JJAS} = 122$  days is the JJAS duration.

#### 149 **e) Indicators of OIV impact**

150 Following Waldman et al. (2018), we introduce two indicators to quantify the impact of OIV on a given variable  
151  $X$ , respectively on the mean state and at the daily scale.

152 The relative intrinsic variability of the temporal mean state of  $X$  over a given period is computed as the ratio  
153 between the ensemble standard deviation  $\sigma_i$  and ensemble average  $m_i$  of the temporal mean  $m_t$  of  $X$  over this  
154 period:

$$155 \quad MI(X) = \frac{\sigma_i(m_t(X(t,i)))}{m_i(m_t(X(t,i)))} \quad (5)$$

156 It quantifies the impact of OIV on the summer mean of  $X$ .

157



158 For each day of JJAS 2018, the intrinsic contribution to the total temporal variability of  $X$  is computed as the ratio  
159 between the time-dependent intrinsic variability and the total temporal variability over JJAS 2018:

$$160 \quad VI(X(t)) = \frac{\sigma_i(X(t,i))}{\sqrt{m_i(\sigma_t(X(t,i))^2)}} \quad (6)$$

161 It quantifies the impact of OIV on the daily variability of  $X$ .

162

### 163 **3. Intraseasonal variability of wind and ocean circulation**

164 The southwest summer monsoon wind blows from June to September over the SCS with three main peaks of  
165 strong northeastward wind (see the daily time series of wind stress averaged over boxOF, boxSC and boxMK,  
166 Figure 2a,b,c): June (9<sup>th</sup>-18<sup>th</sup> June, 10 days), July (28<sup>th</sup> June-18<sup>th</sup> July, 21 days) and August (1<sup>st</sup>-13<sup>th</sup> August, 13  
167 days). Figure 3a,b,c,d shows for each peak the maps of ensemble average of wind stress and wind stress curl, of  
168 surface current speed and of surface current vorticity averaged over the peak period, and the maps of relative  
169 intrinsic variability (MI) of surface current vorticity over the period. A high (low) value of MI of current vorticity  
170 indicates a strong (weak) OIV and a chaotic (stable) circulation. To quantify the strength of the eastward jet, we  
171 calculate the ensemble mean of the average surface current speed through the meridional transect at 109.9°E,  
172 between 9.5 and 12.2°N (see red line on Figure 3a) during the three peaks.

173 During the June peak, the area of strong positive wind stress curl extends from the coast to ~113°E, with a narrow  
174 meridional coverage (Figure 3a). The ACC dipole is not clearly formed (Figure 3b,c). The weak eastward jet is  
175 located in the south with a maximum speed of 0.5-0.7 m.s<sup>-1</sup> around 10-11°N, and a mean strength of 0.51 m.s<sup>-1</sup>.  
176 The circulation is stable in the coastal jet area (MI of current vorticity <50%, Figure 3d), but much more chaotic  
177 over most of the offshore area (MI >200%). During the July period, the area of strong positive wind stress curl is  
178 larger than in June (from 10.5°N to 13°N, extending to 112°E). The eastward jet strengthens, with a mean strength  
179 of 0.78 m.s<sup>-1</sup>, and is more in the north, with a speed of about 0.8-1.1 m.s<sup>-1</sup> near 11-12°N. The ACC dipole, with an  
180 anticyclonic (cyclonic) circulation in the south (north), is more pronounced than in June. The circulation is more  
181 stable than in June in the coastal zone and in the cyclonic and anticyclonic areas (MI of current vorticity ~ 100%).  
182 It is less stable in the northeastern region of boxOF, where MI exceeds 200%. During the August period, the area  
183 of strong positive wind stress curl has the largest meridional and zonal extent, to 114°E. The eastward jet is still  
184 stronger, reaching 1.2-1.5 m.s<sup>-1</sup> around 10.5-11.5°N and a mean strength of 0.88 m.s<sup>-1</sup>. The ACC dipole is also  
185 stronger, with a well-established and large cyclonic gyre. The surface circulation is more stable compared to June  
186 and July, with a larger surface of low MI of current vorticity (<100%) covering boxOF. In September, the summer  
187 monsoon and the large-scale jet/ACC circulation begin to weaken (not shown).

188

### 189 **4. Intraseasonal variability of upwelling**

190 Here we examine the upwelling intraseasonal variability and its intrinsic variability for each upwelling area. Table  
191 1 shows for the four areas the value of yearly upwelling index  $UI_{y,boxN}$  for each member and for the ensemble  
192 average, and its relative intrinsic variability  $MI(UI_{y,boxN})$ . It also shows the values of the correlation coefficients



193 between the daily time series of the ensemble mean of  $UI_{d,boxN}$  and of the wind stress components and intensity.  
194 Figure 2 shows for each upwelling area the daily time series of wind stress, of  $UI_{d,boxN}$  for each simulation and for  
195 the ensemble average, and of  $VI(UI_{d,boxN})$ . Figure 3e,f shows for each summer monsoon peak identified in Section  
196 2 the maps of  $UI_d$  on the day of maximum  $UI_{d,boxN}$  over each peak period and the maps of its relative intrinsic  
197 variability  $MI(UI_d)$ .

### 198 **1. The southern coastal upwelling (SCU)**

199 For SCU,  $UI_{d,boxSC}$  time series show the same daily chronology for each member and for the ensemble mean  
200 (Figure 2b). SCU begins to develop during the first half of June, lasts during the whole summer with a strong  
201 intraseasonal variability, and disappears during the first half of September. We obtain three peaks of similar  
202 intensity, near June 19<sup>th</sup>, July 15<sup>th</sup> and August 16<sup>th</sup>, in phase with the wind forcing over the area: the correlation  
203 between the time series of  $UI_{d,boxSC}$  and of the daily averaged wind stress intensity over boxSC is equal to 0.64  
204 ( $p < 0.01$ , Table 1). The correlation with the wind stress eastward component, i.e. the component nearly parallel to  
205 the south coast, that favors the SCU, reaches 0.71 ( $p < 0.01$ ).

206 Over the summer,  $VI(UI_{d,boxSC})$  varies between 10% when SCU is weak and 40% during periods of strong SCU,  
207 showing similar values for the three upwelling peaks (Figure 2e). The yearly upwelling index  $UI_{y,boxSC}$  shows a  
208 weak ensemble standard deviation (7% relative to the mean, Table 1). This intrinsic variability of the SCU summer  
209 strength is much weaker than its interannual variability: in the 2009-2018 LONG simulation analyzed by To Duy  
210 et al. (2022),  $UI_{y,boxSC}$  shows a 53% interannual standard deviation relative to its interannual mean. SCU develops  
211 in the same area for the ten members, in the coastal zone of the ACC dipole convergence, as shown by the very  
212 low values of  $MI(UI_d)$  (<50%) over this area (Figure 3e,f). Higher  $MI(UI_d)$  values are obtained at the periphery of  
213 this area, along the northern and southern flanks of the eastward jet. They are related to the variability of the  
214 meridional position of the jet: a jet located further north (south) induces a SCU further north (south).

215 SCU daily to intraseasonal variability is therefore mostly driven by the wind. The OIV mainly results from the  
216 meridional position of the jet (that does not vary much), thus affects the SCU at a second order at the intraseasonal  
217 scale.

### 218 **2. The Mekong delta shelf upwelling (MKU)**

219 For MKU, time series of  $UI_{d,boxMK}$  are almost identical for each member and for the ensemble mean (Figure 2c).  
220 They show a strong intraseasonal variability, with three peaks of varying intensity following the three wind peaks.  
221 The July peak is the strongest, followed by the August peak, then the June peak. The daily chronology of MKU  
222 also strongly follows the wind chronology, with a correlation of 0.65 ( $p < 0.01$ ) with the wind stress intensity  
223 averaged over MKU, and of 0.59 (0.61) with the wind stress eastward (northward) component (Table 1).

224 MKU is very weakly influenced by the OIV:  $VI(UI_{y,boxMK})$  never exceeds 30% (Figure 2e) and  $MI(UI_{y,boxMK})$  is  
225 equal to 6% (Table 1). Again, this intrinsic variability of MKU summer strength is negligible compared to its  
226 interannual variability: the interannual standard deviation of  $UI_{y,boxMK}$  is equal to 85% in the LONG simulation  
227 (To Duy et al., 2022). Spatially, MKU is also very stable. As shown by To Duy et al. (2022), it develops along  
228 the northeastward current, in the wake of Con Dao islands (Figures 1, 3e). For the 3 periods of MKU development,



229 Figure 3d,f shows extremely very weak values of MI both for the surface current vorticity and for the spatial  
230 upwelling index. The circulation is therefore extremely stable in this area, explaining the spatial stability of MKU.

231 The daily chronology and intensity of MKU are thus mainly driven by the wind, and its position is determined by  
232 non-varying factors, presumably bathymetry, that still need to be investigated, and not by chaotic factors like  
233 (sub)mesoscale circulation. As a result, MKU is hardly affected by OIV.

### 234 3. The offshore upwelling (OFU)

235 Again, the daily chronology of OFU is very similar for the ten members and the ensemble mean (Figure 2a), and  
236 in phase with the wind chronology (correlation of 0.65,  $p < 0.01$  with the daily wind stress intensity over boxOF,  
237 Table 1). However, contrary to SCU, the intensity of OFU peaks varies throughout the season, though wind stress  
238 intensity is similar during those peaks. We obtain two strong peaks ( $\sim 1.0^\circ\text{C}$ ) in the heart of summer on July 19<sup>th</sup>  
239 and August 13<sup>th</sup>, a moderate peak ( $\sim 0.6^\circ\text{C}$ ) at the end of August, and two small peaks ( $\sim 0.2^\circ\text{C}$ ) at the beginning  
240 and end of summer, on June 18<sup>th</sup> and September 16<sup>th</sup>.  $VI(U_{d,boxOF})$  also varies a lot seasonally, and is maximum  
241 and much stronger than for SCU and MKU during OFU peaks (Figure 2e): it reaches 90% for the July peak, 70%  
242 during the August peaks, and respectively 30% and 50% during the small June and September peaks. On the  
243 summer average,  $MI(U_{y,boxOF})$  is equal to 18% (Table 1), again stronger than for SCU and MKU, but still much  
244 lower than the interannual variability (126%, To Duy et al., 2022). The regional daily wind stress therefore drives  
245 the daily to intraseasonal variability of OFU at the first order. However, OIV also significantly influences this  
246 daily variability, and this influence varies seasonally.

247 To understand the mechanisms that explain the intraseasonal variability of OFU intensity, we examine its  
248 functioning during its three main peaks: June, July and August. Da et al. (2019) and To Duy et al. (2022) showed  
249 that OFU is mainly induced by Ekman pumping and develops in the area of strong positive wind stress curl and  
250 current vorticity. The eastward jet and ACC dipole that favor the development of OFU are much stronger and well  
251 established in the heart of summer than at the beginning and end of the summer monsoon (Figure 3bc and Part 3):  
252 in June and September, contrary to July and August, the area of positive current vorticity over boxOF is indeed  
253 very small and not located over an area of strong positive wind curl, not favoring Ekman pumping (Figure 3e).  
254 The intraseasonal variability of OFU peaks is thus explained by the intraseasonal variability of large-scale  
255 circulation.

256 We then examine the mechanisms that explain why the July and August peaks show different intrinsic variability  
257 but similar ensemble mean of OFU intensity (Figure 2a). Figure 4a shows the maps of  $UI_d$  on the day of maximum  
258  $UI_{d,boxOF}$  over the July OFU peak period and the maps of average surface current vorticity during the this period  
259 for 2 members of strong OFU (13, maximum  $UI_{d,boxOF} = 1.53^\circ\text{C}$ ; 17, maximum  $UI_{d,boxOF} = 1.42^\circ\text{C}$ , Figure 2a)  
260 and 2 members of weak OFU (15, maximum  $UI_{d,boxOF} = 0.77^\circ\text{C}$ ; 18, maximum  $UI_{d,boxOF} = 0.65^\circ\text{C}$ ). In July, the  
261 eastward jet is much stronger than in June (Figure 3b,c and Part3). OFU develops mainly in the area of positive  
262 wind stress curl and current vorticity along the northern flank of the jet (Figures 3c,e and 4). When the position  
263 of the eastward jet is south, as for members 13 and 17, the area where positive current vorticity and positive wind  
264 curl coincide is larger than average, favoring Ekman pumping. This results in a stronger OFU, with a larger  
265 extension to the northeast. This is the opposite when the position of the eastward jet is north (members 15 and  
266 18). Figure 3d,f shows strong values of MI of current vorticity and upwelling intensity ( $> 100\%$ ) along the





267 eastward jet and in the northeast area of boxOF. This confirms that OFU intrinsic variability in July is related to  
268 the effect of eastward jet meridional position variability on the circulation and on the upwelling that develops  
269 along the northern flank of the jet. Figure 4b shows the maps of  $UI_d$  on the day of maximum  $UI_{d,boxOF}$  over the  
270 August OFU peak period and the maps of average surface current vorticity and average wind stress curl during  
271 this period for 2 members of strong OFU (14, maximum  $UI_{d,boxOF} = 1.65$  °C; 13, maximum  $UI_{d,boxOF} = 1.20$  °C,  
272 Figure 2a) and 2 members of weak OFU (10, maximum  $UI_{d,boxOF} = 0.82$  °C; 16, maximum  $UI_{d,boxOF} = 0.89$  °C).  
273 In August, part of OFU still develops in the area of positive surface current vorticity along the northern flank of  
274 the eastward jet, but to a lesser extent than in July (Figures 3e, 4). The meridional position of the jet does not vary  
275 a lot from one member to another (Figure 4b), as confirmed by the lower values of MI of current vorticity in the  
276 jet area (Figure 3d). The eastward jet is thus stronger and more stable than in July (Figure 3b,c and Part 3), and  
277 does not induce a strong intrinsic variability of OFU. Instead, August OFU mainly develops in the area of positive  
278 vorticity north of the jet associated with the cyclonic eddy of the ACC dipole (Figures 4b,3e). The variations of  
279 zonal position of this eddy explain the variability of OFU intensity. From members 14, to 13, 10 and 16, this eddy  
280 is located more and more to the east, i.e. further and further away from the area of strong positive wind stress curl,  
281 resulting in a weaker and weaker OFU (Figures 4b). The variability of circulation in the northern part of boxOF  
282 therefore explains OFU intrinsic variability in August. This variability is moreover lower than in July: MI of  
283 current vorticity and of  $UI_d$  in this northern part (highlighted by the black triangle in Figure 3d,e,f) is lower in  
284 August than in July. The more stable jet in August, that results in a smaller intrinsic variability of OFU along the  
285 jet, and the smaller intrinsic variability of current vorticity in the northern cyclonic part, where OFU mostly  
286 develops, therefore explain the intrinsic variability of OFU in August and the fact that it is smaller than in July.

#### 287 **4. The northern coastal upwelling (NCU)**

288 The ten members and the ensemble mean simulate NCU with a strong intraseasonal variability and a similar  
289 chronology (Figure 2d), completely different from the chronology obtained for the three other areas. A strong  
290 NCU develops at the beginning of the summer (from June 10<sup>th</sup> to July 4<sup>th</sup>, reaching ~1.2°C for the ensemble  
291 average), and a weak NCU develops at the end of August (August 26<sup>th</sup> to 31<sup>st</sup>, reaching ~0.2°C). During those  
292 periods, NCU chronology follows the wind chronology for the ten members:  $UI_{d,boxNC}$  peaks correspond to peaks  
293 of northward (i.e. alongshore) wind favorable to NCU, around June 18<sup>th</sup> and 25<sup>th</sup>, July 2<sup>nd</sup>, and August 28<sup>th</sup>  
294 and 29<sup>th</sup>. There still a significant correlation between the time series of  $UI_{d,boxNC}$  and the time series of wind stress  
295 northward component over boxNC, that favors the Ekman upwelling in this area (0.37,  $p < 0.01$ , Table 1). It is  
296 however much weaker than correlations obtained for the other areas (at least 0.64). Moreover, although northward  
297 wind peaks occur during the whole summer, NCU does not develop from mid-July to mid-August.

298 NCU shows the strongest OIV of the four areas.  $VI(UI_{d,boxNC})$  reaches 170% during the June-July peak, and is  
299 much smaller during the rest of the summer, reaching at most ~80% during the short late August peak (Figure 2e).  
300 The strong OIV in June explains the strong OIV at the summer scale (Table 1):  $MI(UI_{s,boxNC})$  is equal to 37%,  
301 twice larger than for OFU and ~6 times larger than for SCU and MKU. It is of the same order of magnitude as the  
302 interannual variability of MKU summer strength, even if twice smaller (72% in the LONG simulation, To Duy et  
303 al., 2022).



304 These results suggest that the daily to intraseasonal chronology of upwelling in boxNC is partly driven by wind,  
305 but to a lesser extent than in the other areas, and that other factors are involved that induce a strong intrinsic  
306 variability of NCU both at the daily and summer scales. To identify those factors, we examine three periods: the  
307 period of strong wind over boxNC and strong NCU in June (June 10<sup>th</sup> – July 4<sup>th</sup>), the period of strong wind but no  
308 NCU in July (July 17<sup>th</sup> - 22<sup>nd</sup>), and the period of strong wind and weak NCU at the end of August (August 26<sup>th</sup> -  
309 31<sup>st</sup>). We show in Figure 5 the maps of ensemble average of average surface current, current vorticity and MI of  
310 current vorticity over each period, and the maps of  $UI_d$  and  $MI(UI_d)$  on the day of maximum  $UI_{d,boxNC}$  over each  
311 period.

312 During the June event, ensemble average circulation in and around boxNC is globally offshore oriented. This  
313 favors the Ekman transport, hence the development of NCU. The ensemble spreading of NCU strength is very  
314 strong:  $MI(UI_d)$  spatially reaches 500% in the eastern part of boxNC (Figure 5e), and  $VI(UI_{d,boxNC})$  reaches 170%  
315 (Figure 2e). Figure 6 shows the maps of wind speed and curl, current speed and vorticity and  $UI_d$  on the day of  
316 maximum  $UI_{d,boxNC}$  over the June wind peak period for two members of strong NCU (10 and 16) and two members  
317 of weak NCU (09 and 11). A cyclonic gyre in the north and anticyclonic gyre in the south meet in boxNC for  
318 members 10 (between 13°N and 14°N) and 16 (between 14°N and 15°N). This induces a convergence and an  
319 offshore current resulting in a strong upwelling, following the same mechanism as for SCU. For members 09 and  
320 11, cyclonic and anticyclonic gyres do not meet in boxNC, but either north or south of boxNC, not inducing  
321 offshore oriented current over boxNC. Instead a weak NCU is induced by a favorable northward alongshore  
322 current in the northern part of boxNC (Figure 6). As already observed at the interannual scale by To Duy et al.  
323 (2022) for the interannual variability, mesoscale circulation of strongly chaotic nature in and around boxNC  
324 therefore drives the NCU development and explains its high intrinsic variability during the June period.

325 Between mid-July and mid-August, the large-scale circulation (ACC dipole and eastward jet) is strongly  
326 established (see Parts 3 and 4c). The western part of the cyclonic eddy covers boxNC and induces a strong  
327 southward alongshore current over this region. Close to the coast, this alongshore current is associated with a  
328 divergent circulation, hence with a coastward component and a coastal downwelling which inhibits the NCU (see  
329 the high negative vorticity in this area in Figure 5b). This large-scale ocean circulation is common for the ten  
330 members and systematically prevents the NCU to develop (see the weak MI of current vorticity and the weak  
331 upwelling in Figure 5). This explains the very weak  $UI_{d,boxNC}$  and  $VI(UI_{d,boxNC})$  during this period (Figure 2e).

332 During the August event, the average circulation is similar to the mid-July and mid-August circulation described  
333 above (Figure 5a,b). However, with the weakening of the summer monsoon, the ACC dipole structure  
334 progressively weakens, the negative vorticity is less strong and the current is a bit more offshore oriented: NCU  
335 is not as strong as in June, but it can develop easier than in the middle of the summer.  $VI(UI_{d,boxNC})$  consequently  
336 increases, but stays smaller than in June.

337 Our results therefore show that the development of NCU at the intraseasonal scale is first related to the large-scale  
338 circulation (eastward jet + ACC dipole). When this circulation is strongly established during the heart of summer,  
339 it prevents the NCU from developing. NCU is only allowed to develop at the beginning and end of summer, when  
340 this circulation is weaker. Then, inside those periods of “allowed NCU development”, the daily chronology and



341 the intensity of NCU are first driven by the alongshore component of wind, but also by the organization of  
342 mesoscale circulation in and around boxNC that explains its very strong intrinsic variability.

343

## 344 **5. Conclusion and future work**

345 An ensemble of ten fine-resolution simulations with perturbed initial conditions was performed and analyzed in  
346 this paper to represent and investigate the daily to intraseasonal variability of ocean circulation and of SVU over  
347 its different areas of development and the influence of OIV.

348 The ensemble was used to examine the seasonal variability and intrinsic variability of the circulation in the SVU  
349 region during summer 2018. In June, the eastward jet is weak and mainly located in the south, the ACC dipole is  
350 not formed and the circulation is only stable in the coastal area. In July, the jet is stronger and the ACC dipole is  
351 clearly formed. The circulation in the area of positive vorticity north of the jet is more stable. In August southwest  
352 monsoon wind is the strongest and has the largest area of influence, inducing an even stronger eastward jet and a  
353 pronounced ACC dipole. The circulation is stable over a larger area than in July.

354 We then examined the seasonal variability and intrinsic variability of the upwelling.

355 For SCU, MKU and OFU, the daily chronology and intraseasonal variability of the upwelling are quite similar  
356 and mainly driven by the summer monsoon wind, with upwelling maxima in phase with strong southwest wind  
357 periods. Their intrinsic variability is much weaker than their interannual variability.

358 The development of MKU and SCU is related to ocean circulation processes, respectively the northeastward  
359 current and eastward jet, that are spatially quite stable. As a result, MKU and SCU show a very weak intrinsic  
360 variability, both at the daily scale and on average over the summer (lower than 10%), both spatially and on average  
361 over the area. Peaks of OIV are related to peaks of upwelling intensity. SCU develops as long as wind conditions  
362 are favorable over the area of the ACC dipole convergence, that does not vary much spatially. MKU develops  
363 along the northeastward current that flows offshore the Mekong delta and is spatially very stable.

364 OFU shows a stronger intrinsic variability, both at the daily scale and for the summer average (18%), both spatially  
365 and on average over boxOF. The seasonal variability of OFU intensity and intrinsic variability are not only driven  
366 by the wind, but also related to the period of the season. The large-scale circulation (ACC dipole and eastward  
367 jet) that enhances the Ekman pumping – induced OFU is weak in June and September, whereas it is strongly  
368 established in the heart of summer in July and August. This explains the stronger OFU intensity and OIV during  
369 the July-August period. Moreover, for similar OFU intensity, the impact of OIV is weaker in August than in July.  
370 In July, OFU mainly develops along the northern flank of the eastward jet. The meridional position of this jet is  
371 quite variable, explaining the strong intrinsic variability of the July OFU: a southern (northern) position of the jet  
372 induces a larger (smaller) common area between positive curl of wind stress and current, hence induces a stronger  
373 (weaker) upwelling. In August, this position is much more stable. Moreover, OFU mainly develops in the area of  
374 cyclonic activity north of the jet, related to mesoscale eddies of strong chaotic nature. OFU intensity depends on  
375 the zonal position of this cyclonic activity with respect to the wind curl: a cyclonic eddy (not) located in the area



376 of strong positive wind stress curl results in stronger (weaker) OFU. The circulation in this area is moreover more  
377 stable than in July, explaining the weaker intrinsic variability in August.

378 NCU daily chronology and the intraseasonal variability is completely different from the other areas, and its  
379 intrinsic variability is much higher. At the intraseasonal scale, the development of NCU is driven by the large-  
380 scale circulation. During the heart of summer, from mid-July to end of August, the eastward jet and ACC dipole  
381 are strongly established, inducing a strong southward alongshore current over boxNC which annihilates NCU,  
382 explaining its very low intensity and intrinsic variability. At the beginning and, to a smaller extent, end of summer,  
383 the large-scale ACC dipole structure and associated eastward current are weaker, allowing offshore current to  
384 develop. Inside these periods, NCU chronology is driven by the wind but also by the development (or not) of  
385 offshore oriented currents related to the spatial organization of coastal eddies. NCU shows a strong intrinsic  
386 variability related to the strong chaotic variability of those small mesoscale structures, of the same order as its  
387 interannual variability (37%).

388 We investigated here the role of OIV on the circulation and upwelling in the SVU region. Further studies are now  
389 required to investigate the influence of other factors, including tides and rivers. We moreover developed an ocean-  
390 atmosphere regional coupled model that will allow to study the impact of upwelling on atmosphere and climate,  
391 at local and regional scales, that was studied until now using satellite data and an atmosphere-only model (Xie et  
392 al. 2003; Zheng et al., 2016; Yu et al., 2020). The impact of upwelling on the marine ecosystem should also be  
393 studied, using for example the dynamical-biogeochemical coupled model developed by Ulses et al. (2016) and  
394 Herrmann et al. (2017). Finally, the long-term evolution of the upwelling should be studied, in particular since  
395 Herrmann et al. (2020,2022) showed that summer monsoon winds may weaken in response to climate change.  
396 Last, the upwelling that develops offshore the Mekong Delta, MKU, was revealed by To Duy et al. (2022) and  
397 confirmed by the present study, and the northern coastal upwelling, NCU, was revealed by Da et al. (2019) and  
398 confirmed by Ngo and Hsin (2021). Extremely few in-situ observations are available over their areas and periods  
399 of development, and field campaigns are therefore necessary to better understand their functioning. This study  
400 explored the impact of OIV on the South Vietnam Upwelling, but is more generally of interest for the scientific  
401 community working on the functioning and variability of upwellings and on the effect and modeling of OIV.

402

#### 403 **Code and data availability**

404 The SYMPHONIE model is available on the webpage of the SIROCCO group, <https://sirocco.obs-mip.fr/>. Sea  
405 surface temperature, currents and windstress simulated by the ensemble over summer 2018 are freely available  
406 on <https://doi.org/10.5281/zenodo.7504087>.

407

#### 408 **Authors Contribution**

409 Marine Herrmann, To Duy Thai and Claude Estournel designed the experiments and To Duy Thai carried them  
410 out. Marine Herrmann prepared the manuscript with contributions from all co-authors.

411



412 **Competing interests**

413 The authors declare that they have no conflict of interest.

414

415 **Acknowledgements**

416 This work is a part of LOTUS international joint laboratory (lotus.usth.edu.vn). PhD studies of To Duy Thai were  
 417 funded through an IRD ARTS grant and a “Bourse d’Excellence” from the French Embassy in Vietnam.  
 418 Numerical simulations were performed using CALMIP HPC facilities (project P13120) and the cluster OCCIGEN  
 419 from the CINES group (project DARI A0080110098). This paper is a contribution to celebrate the 100 years  
 420 Anniversary of the Institute of Oceanography, Vietnam Academy of Science and Technology.

421

422 **Tables**

423 Table 1 : For each upwelling area: value of the yearly upwelling index  $UI_{y,boxN}$  for each member of the ensemble,  
 424 of the ensemble mean  $m_i(UI_{y,boxN})$  and of  $MI(UI_{y,boxN})$ , and correlation coefficients between the daily times  
 425 series of the ensemble mean of the daily upwelling index  $UI_{d,boxN}$  and of the wind stress eastward and northward  
 426 components and intensity. Only correlations associated with p-values <0.01 are shown.

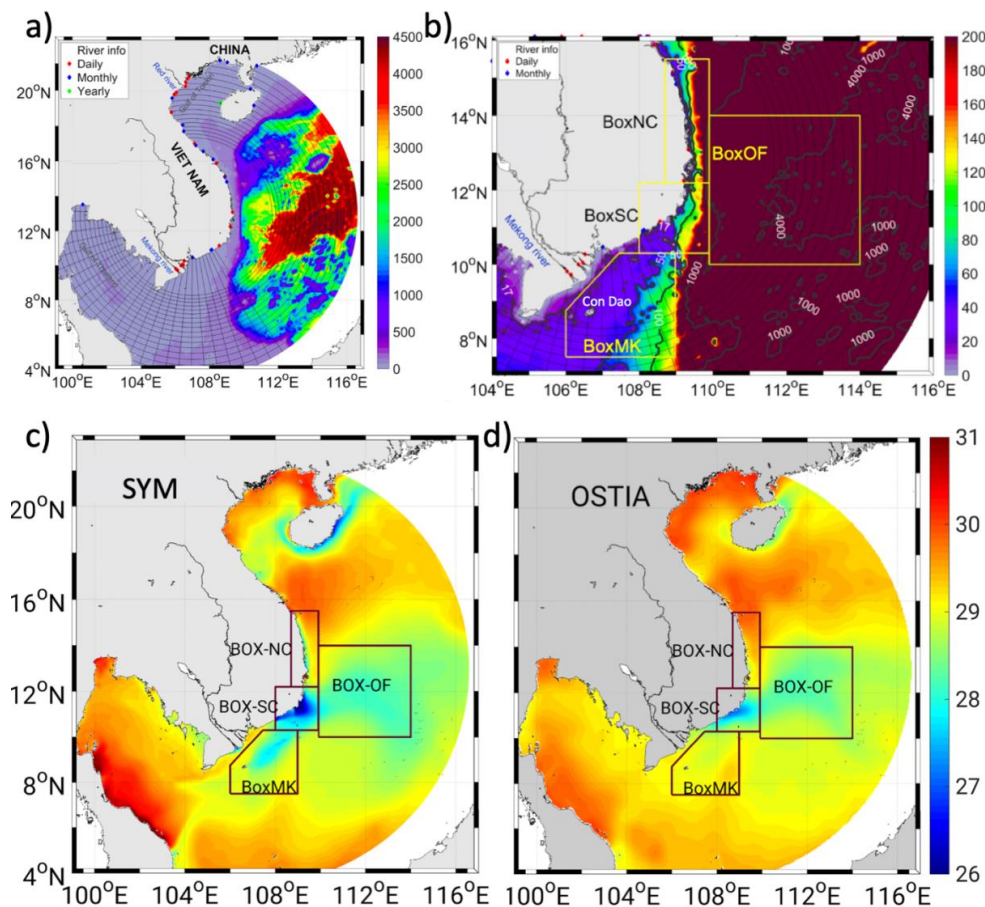
Members	09	10	11	12	13	14	15	16	17	18	$m_i(UI_{y,boxN})$ (°C)	$MI(UI_{y,boxN})$ (%)	Correlation between $m_i(UI_{d,boxN})$ and wind stress eastward component	Correlation between $m_i(UI_{d,boxN})$ and wind stress northward component	Correlation between $m_i(UI_{d,boxN})$ and wind stress intensity
BoxOF	0.32	0.35	0.26	0.39	0.37	0.39	0.26	0.26	0.42	0.31	0.33	18 %	0.62	0.62	0.65
BoxSC	1.25	1.35	1.25	1.49	1.39	1.42	1.27	1.38	1.48	1.29	1.36	7 %	0.60	0.71	0.64
BoxNC	0.11	0.24	0.08	0.15	0.17	0.14	0.25	0.25	0.26	0.13	0.18	37 %	--	0.37	--
BoxMK	0.18	0.18	0.19	0.19	0.17	0.18	0.17	0.18	0.2	0.17	0.18	6 %	0.59	0.61	0.65

427



428 **Figures**

429



430

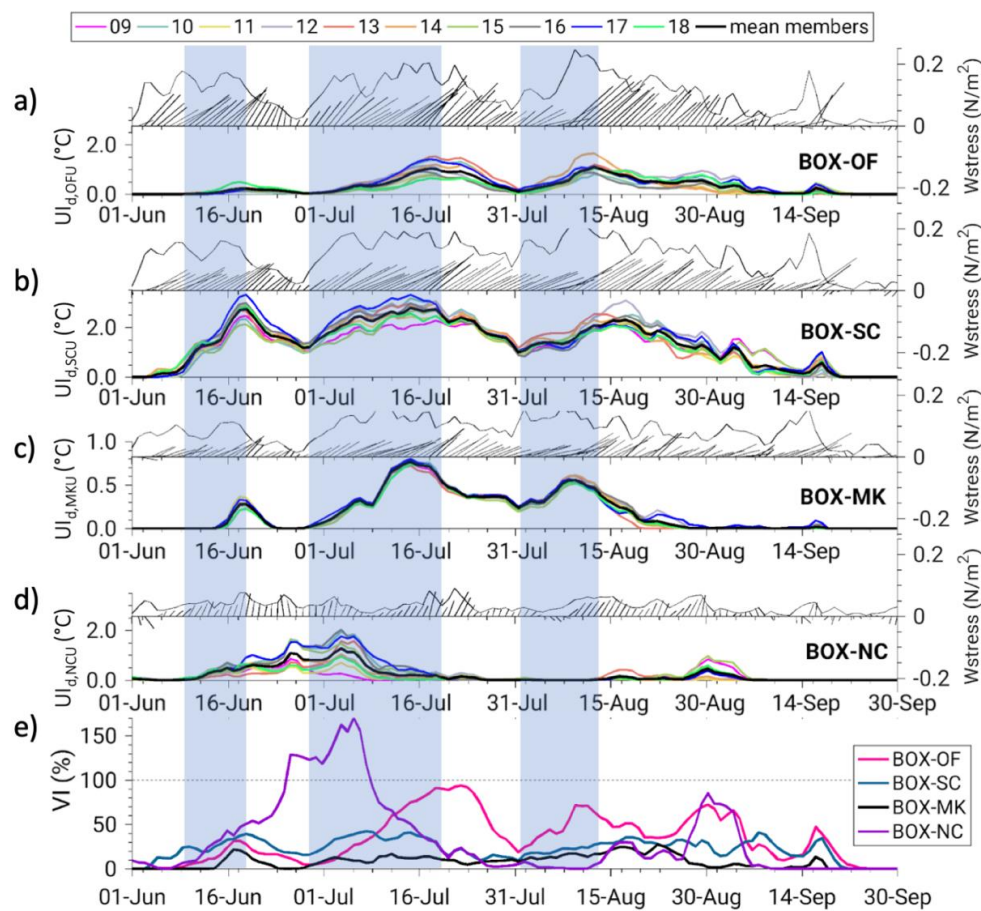
431

432 Figure 1: (a) Characteristics of the orthogonal curvilinear computational grid (black lines, not all the mesh points  
 433 are shown for visibility purposes) and bathymetry (colors, meter, *GEBCO\_2014*) used for the VNC configuration  
 434 of the SYMPHONIE model. Dots show the location of rivers for which we used daily (red), monthly (blue) and  
 435 yearly climatology (green) discharge values (see To Duy et al. 2022 for more details). (b) Bathymetry (meter)  
 436 over the SVU region. The 4 boxes used for the study of SVU are displayed in yellow. (c,d) SST (°C) averaged  
 437 over JJAS 2018 computed from the SYMPHONIE ensemble average (c) and from OSTIA reanalysis (d).

438

439

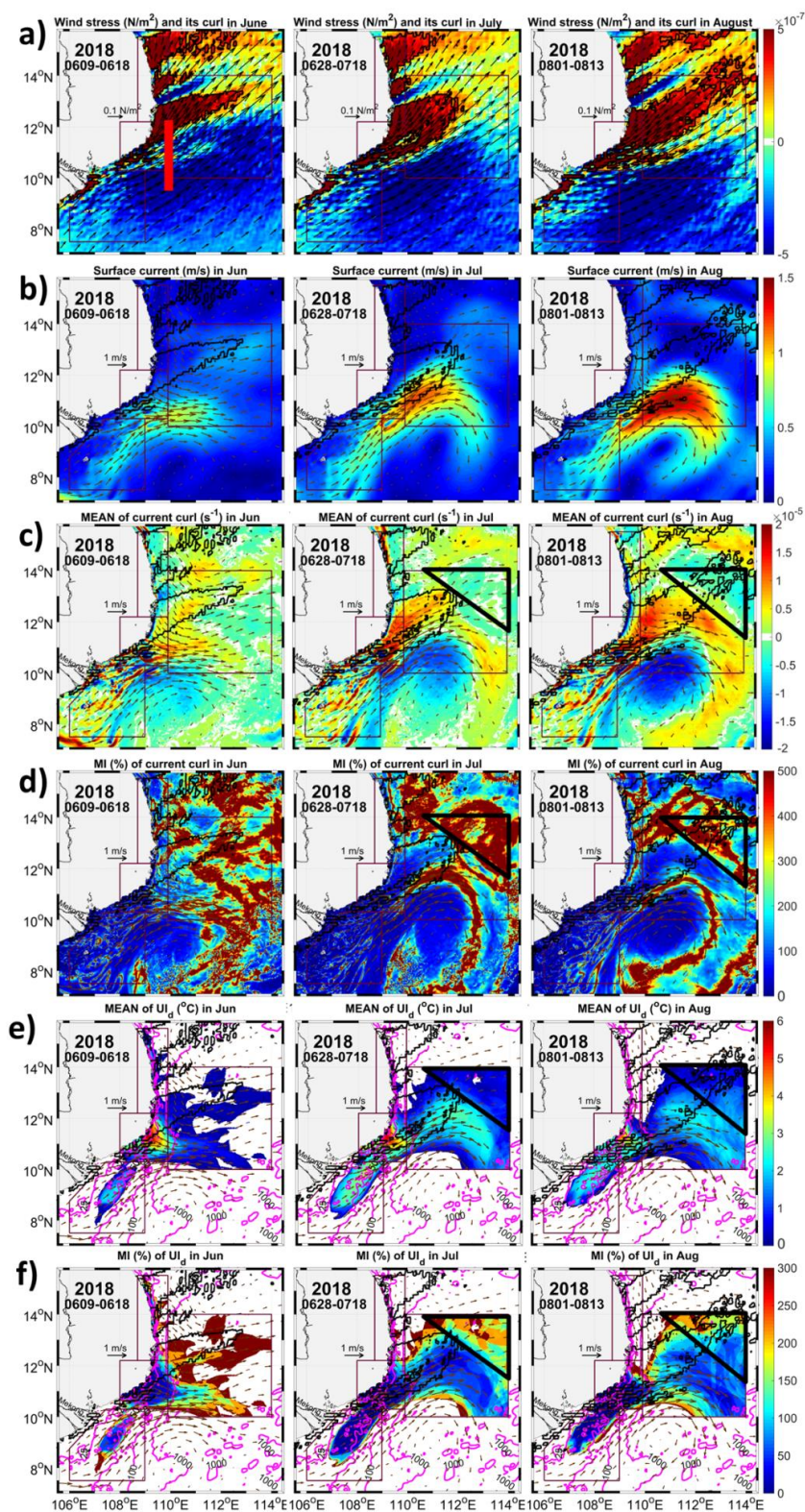




440

441 Figure 2: (a,b,c,d) Daily time series between June 1<sup>st</sup> and September 30<sup>th</sup> 2018 of direction (arrows) and intensity  
 442 (black line) of spatially averaged wind stress (N·m<sup>-2</sup>) over each upwelling area, and time series of  $UI_{d,boxN}$  for each  
 443 simulation (colored lines) and for the ensemble average (black thick line) for each upwelling area (a, BoxSC; b,  
 444 BoxOF; c, BoxMK; d, BoxNC). (e) Daily time series of  $VI(UI_{d,boxN})$  for each upwelling area. Periods of southwest  
 445 monsoon wind peaks are highlighted in blue.

446





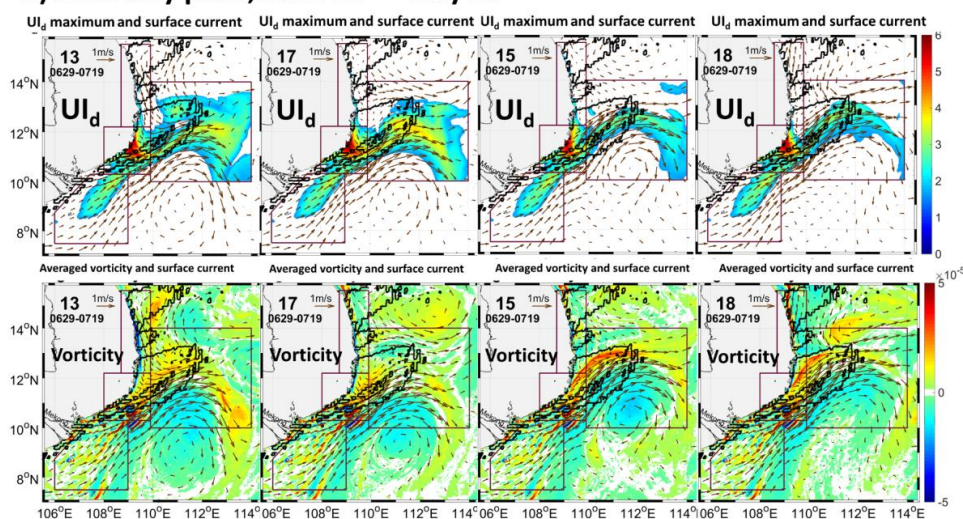


448 Figure 3: Maps of ensemble average of average wind stress (a, arrows,  $\text{N}\cdot\text{m}^{-2}$ ) and wind stress curl (a, colors,  $\text{N}\cdot\text{m}^{-3}$ ), of average surface current speed (b,  $\text{m}\cdot\text{s}^{-1}$ ) and vorticity (c,  $\text{s}^{-1}$ ), of  $UI_d$  (e,  $^{\circ}\text{C}$ ) on the day of maximum  $UI_{d,boxOF}$   
449  $^3$ ), of average surface current speed (b,  $\text{m}\cdot\text{s}^{-1}$ ) and vorticity (c,  $\text{s}^{-1}$ ), of  $UI_d$  (e,  $^{\circ}\text{C}$ ) on the day of maximum  $UI_{d,boxOF}$   
450 over each wind peak period (left June, middle July and right August), and maps of relative intrinsic variability  
451 (MI) of average surface current vorticity (d, %) and of  $UI_d$  (f, %) over each period. Black lines:  $3\cdot 10^{-7} \text{N}\cdot\text{m}^{-3}$  iso-  
452 contours of average wind stress curl. Red segment (a): meridional transect at  $109.9^{\circ}\text{E}$ ,  $9.5 - 12.2^{\circ}\text{N}$  used to  
453 compute the eastward jet strength. Arrows (b-f): average surface current during each period. Black triangles (c-f):  
454 area of high current vorticity northern of the eastward jet during the July and August periods. Pink lines (e, f):  
455 isobaths (meters).

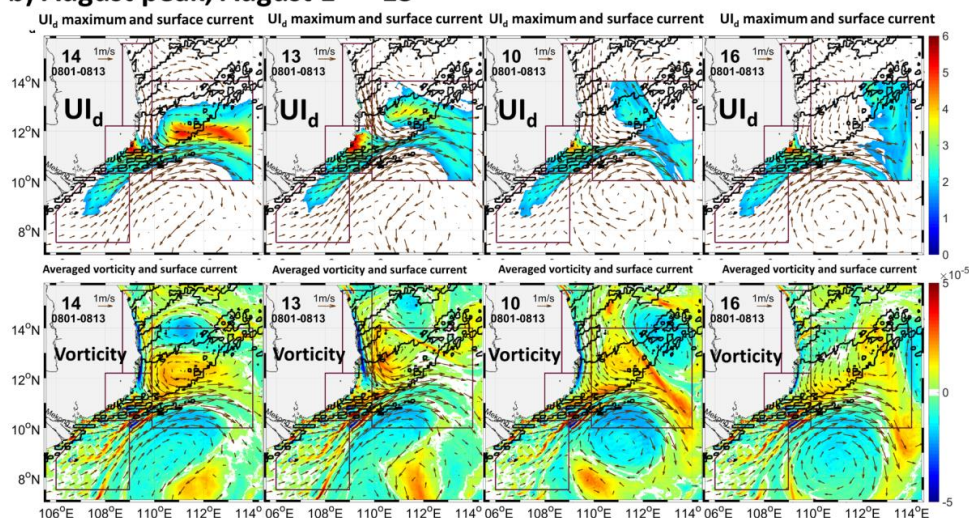
456



**a) June-July peak, June 29<sup>th</sup> – July 19<sup>th</sup>**



**b) August peak, August 1<sup>st</sup> – 13<sup>th</sup>**



457

458

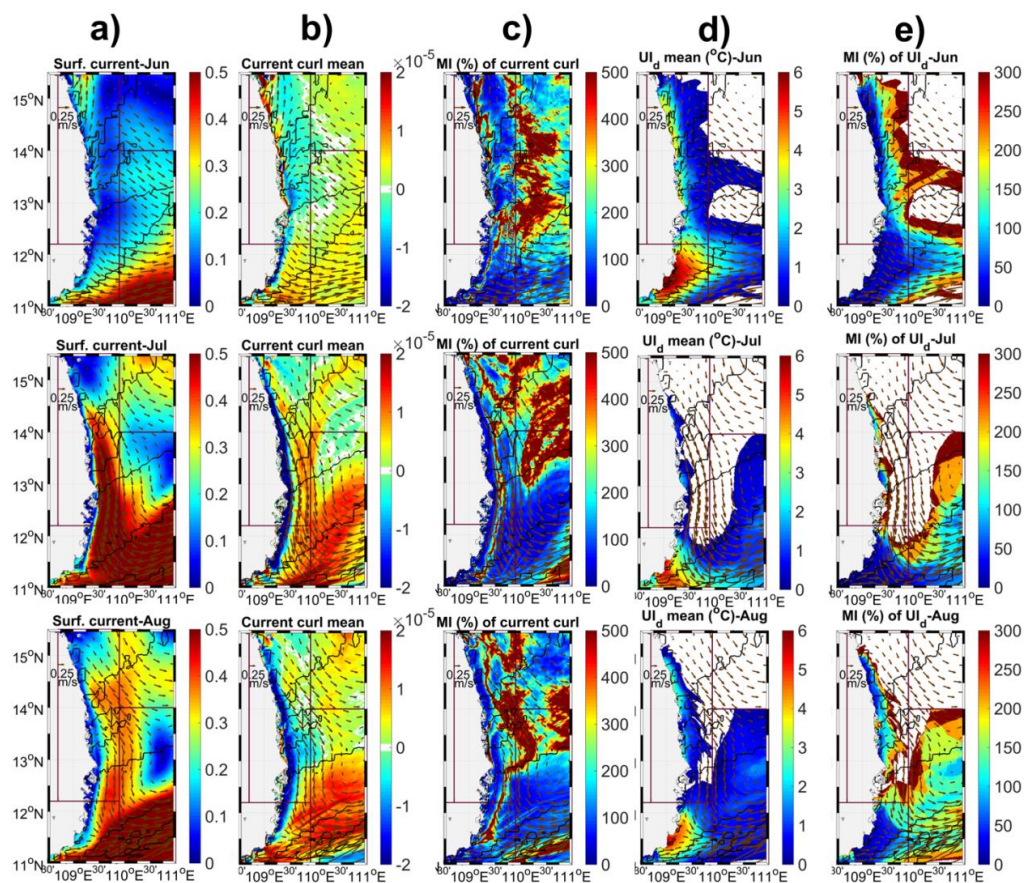
459 Figure 4: Maps of  $UI_d$  (top, °C) on the day of maximum  $UI_{d,boxOF}$  over the (a) July and (b) August peaks of OFU,  
 460 and of average surface current vorticity (bottom,  $s^{-1}$ ) during each peak for 2 members of strong OFU (members  
 461 13 and 17 for July, members 14 and 13 for August, Figure 2a) and 2 members of weak OFU (members 15 and 18  
 462 for July, members 10 and 16 for August). Black contours:  $3 \cdot 10^{-7} N \cdot m^{-3}$  iso-contours of average wind stress curl  
 463 during each period. Arrows: average surface current ( $m \cdot s^{-1}$ ).

464

465



466



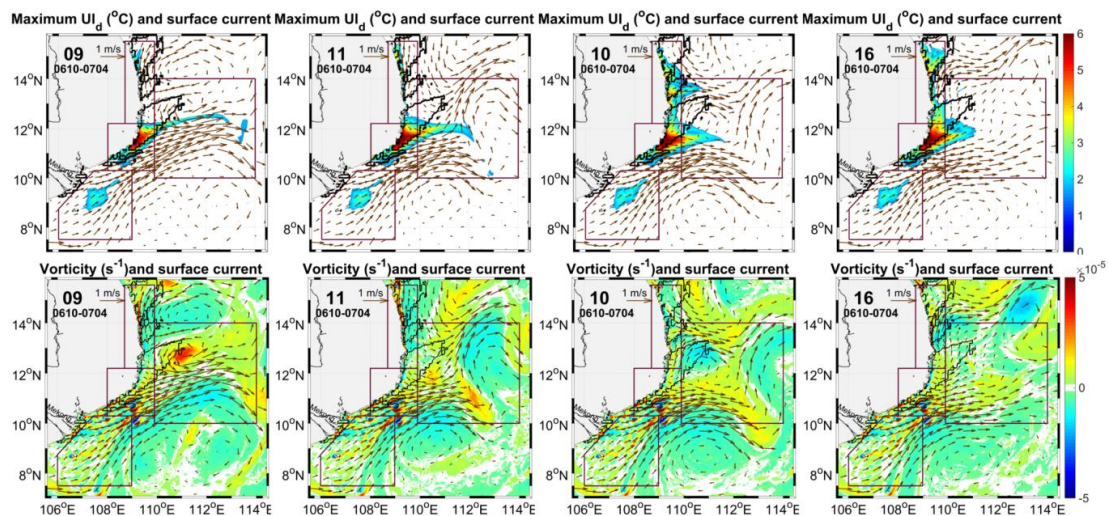
467

468 Figure 5 : Maps of ensemble average of average surface current speed (a,  $m.s^{-1}$ ) and vorticity (b,  $s^{-1}$ ) over each  
 469 wind peak period over BoxNC (1<sup>st</sup> row June 10<sup>th</sup> – July 4<sup>th</sup>, 2<sup>nd</sup> row July 17<sup>th</sup> - 22<sup>nd</sup> and 3<sup>rd</sup> row August 26<sup>th</sup> - 31<sup>st</sup>),  
 470 of  $UI_d$  (d,  $^{\circ}C$ ) on the day of maximum  $UI_{d,BoxNC}$  over each period, and of relative intrinsic variability MI of average  
 471 surface current vorticity (c, %) and  $UI_d$  (e, %) over each period. Black contours:  $3.10^{-7} N.m^{-3}$  iso-contours of  
 472 average wind stress curl during each period. Arrows: average surface current ( $m.s^{-1}$ ).





473



474

475

476 Figure 6 : Maps of  $UI_d$  (1<sup>st</sup> row, °C) on the day of maximum  $UI_{d,boxNC}$  over the July wind peak period over BoxNC  
477 and maps of average surface current vorticity (2<sup>nd</sup> row,  $s^{-1}$ ) for 2 members of weak NCU (9, 11) and 2 members  
478 of strong NCU (10, 16) during the June-July period. Black contours:  $3 \cdot 10^{-7} N \cdot m^{-3}$  iso-contours of average wind  
479 stress curl during each period. Arrows: average surface current ( $m \cdot s^{-1}$ ).

480



481 **References**

- 482 Bombar, D., Dippner, J. W., Doan, H. N., Ngoc, L. N., Liskow, I., Loick-Wilde, N., and Voss, M.: Sources of  
483 new nitrogen in the Vietnamese upwelling region of the South China Sea, *J. Geophys. Res. Ocean.*, 115, 6018,  
484 <https://doi.org/10.1029/2008JC005154>, 2010.
- 485 Chen, C. and Wang, G.: Interannual variability of the eastward current in the western South China Sea associated  
486 with the summer Asian monsoon, *J. Geophys. Res. Ocean.*, 119, 5745–5754,  
487 <https://doi.org/10.1002/2014JC010309>, 2014.
- 488 Chen, C., Lai, Z., Beardsley, R. C., Xu, Q., Lin, H., and Viet, N. T.: Current separation and upwelling over the  
489 southeast shelf of Vietnam in the South China Sea, *J. Geophys. Res. Ocean.*, 117, 1–16,  
490 <https://doi.org/10.1029/2011JC007150>, 2012.
- 491 Da, N. D., Herrmann, M., Morrow, R., Niño, F., Huan, N. M., and Trinh, N. Q.: Contributions of Wind, Ocean  
492 Intrinsic Variability, and ENSO to the Interannual Variability of the South Vietnam Upwelling: A Modeling  
493 Study, *J. Geophys. Res. Ocean.*, 124, 6545–6574, <https://doi.org/10.1029/2018JC014647>, 2019.
- 494 Dippner, J. W., Nguyen, K. V., Hein, H., Ohde, T., and Loick, N.: Monsoon-induced upwelling off the Vietnamese  
495 coast, *Ocean Dyn.*, 57, 46–62, <https://doi.org/10.1007/S10236-006-0091-0>, 2007.
- 496 Herrmann, M., Auger, P. A., Ulses, C., and Estournel, C.: Long-term monitoring of ocean deep convection using  
497 multisensors altimetry and ocean color satellite data, *J. Geophys. Res. Ocean.*, 122, 1457–1475,  
498 <https://doi.org/10.1002/2016JC011833>, 2017.
- 499 Herrmann, M., Ngo-Duc, T., and Trinh-Tuan, L.: Impact of climate change on sea surface wind in Southeast Asia,  
500 from climatological average to extreme events: results from a dynamical downscaling, *Clim. Dyn.* 2020 543,  
501 54, 2101–2134, <https://doi.org/10.1007/S00382-019-05103-6>, 2020.
- 502 Herrmann, M., Nguyen-Duy, T., Ngo-Duc, T., and Tangang, F.: Climate change impact on sea surface winds in  
503 Southeast Asia, *Int. J. Climatol.*, 42, 3571–3595, <https://doi.org/10.1002/JOC.7433>, 2022.
- 504 Isoguchi, O., and Kawamura, H.: MJO-related summer cooling and phytoplankton blooms in the South China Sea  
505 in recent years, *Geophys. Res. Lett.*, 33, L16615, doi:10.1029/2006GL027046, 2006.
- 506 Kuo, N. J., Zheng, Q., and Ho, C. R.: Response of Vietnam coastal upwelling to the 1997-1998 ENSO event  
507 observed by multisensor data, *Remote Sens. Environ.*, 89, 106–115, <https://doi.org/10.1016/j.rse.2003.10.009>,  
508 2004.
- 509 Li, Y., Han, W., Wilkin, J. L., Zhang, W. G., Arango, H., Zavala-Garay, J., Levin, J., and Castruccio, F. S.:  
510 Interannual variability of the surface summertime eastward jet in the South China Sea, *J. Geophys. Res.*  
511 *Ocean.*, 119, 7205–7228, <https://doi.org/10.1002/2014JC010206>, 2014.
- 512 Liu, X., Wang, J., Cheng, X., and Du, Y.: Abnormal upwelling and chlorophyll-a concentration off South Vietnam  
513 in summer 2007, *J. Geophys. Res. Ocean.*, 117, 2–11, <https://doi.org/10.1029/2012JC008052>, 2012.
- 514 Loick-Wilde, N., Bombar, D., Doan, H. N., Nguyen, L. N., Nguyen-Thi, A. M., Voss, M., and Dippner, J. W.:  
515 Microplankton biomass and diversity in the Vietnamese upwelling area during SW monsoon under normal  
516 conditions and after an ENSO event, *Prog. Oceanogr.*, 153, 1–15,  
517 <https://doi.org/10.1016/j.pocean.2017.04.007>, 2017.
- 518 Lu, W., Oey, L. Y., Liao, E., Zhuang, W., Yan, X. H., and Jiang, Y.: Physical modulation to the biological  
519 productivity in the summer Vietnam upwelling system, *Ocean Sci.*, 14, 1303–1320,  
520 <https://doi.org/10.5194/OS-14-1303-2018>, 2018.



- 521 Lyard, F., Lefevre, F., Letellier, T., and Francis, O.: Modelling the global ocean tides: modern insights from  
522 FES2004, *Ocean Dyn.* 2006 565, 56, 394–415, <https://doi.org/10.1007/S10236-006-0086-X>, 2006.
- 523 Marsaleix, P., Auclair, F., Floor, J. W., Herrmann, M. J., Estournel, C., Pairaud, I., and Ulses, C.: Energy  
524 conservation issues in sigma-coordinate free-surface ocean models, *Ocean Model.*, 20, 61–89,  
525 <https://doi.org/10.1016/j.ocemod.2007.07.005>, 2008.
- 526 Marsaleix, P., Michaud, H., and Estournel, C.: 3D phase-resolved wave modelling with a non-hydrostatic ocean  
527 circulation model, *Ocean Model.*, 136, 28–50, <https://doi.org/10.1016/J.OCEMOD.2019.02.002>, 2019.
- 528 Ngo, M. H. and Hsin, Y. C.: Impacts of Wind and Current on the Interannual Variation of the Summertime  
529 Upwelling Off Southern Vietnam in the South China Sea, *J. Geophys. Res. Ocean.*, 126, e2020JC016892,  
530 <https://doi.org/10.1029/2020JC016892>, 2021.
- 531 Pairaud, I., Lyard, F., Auclair, F., Letellier, T., and Marsaleix, P.: Dynamics of the semi-diurnal and quarter-  
532 diurnal internal tides in the Bay of Biscay. Part 1: Barotropic tides, *Cont. Shelf Res.*, 28, 1294–1315,  
533 <https://doi.org/10.1016/J.CSR.2008.03.004>, 2008.
- 534 Pairaud, I., Staquet, C., Sommeria, J., and Mahdizadeh, M. M.: Generation of harmonics and sub-harmonics from  
535 an internal tide in a uniformly stratified fluid: Numerical and laboratory experiments, 28, 51–62,  
536 [https://doi.org/10.1007/978-94-007-0360-5\\_COVER/](https://doi.org/10.1007/978-94-007-0360-5_COVER/), 2010.
- 537 Sérazin, G., Meyssignac, B., Penduff, T., Terray, L., Barnier, B., and Molines, J. M.: Quantifying uncertainties  
538 on regional sea level change induced by multidecadal intrinsic oceanic variability, *Geophys. Res. Lett.*, 43,  
539 8151–8159, <https://doi.org/10.1002/2016GL069273>, 2016.
- 540 To Duy, T., Herrmann, M., Estournel, C., Marsaleix, P., Duhaut, T., Bui Hong, L., and Trinh Bich, N.: Role of  
541 wind, mesoscale dynamics and coastal circulation in the interannual variability of South Vietnam Upwelling,  
542 South China Sea. Answers from a high resolution ocean model, *Ocean Sci.*, 18, 1131–  
543 1161, <https://doi.org/10.5194/os-18-1131-2022>, 2022
- 544 Ulses, C., Auger, P. A., Soetaert, K., Marsaleix, P., Diaz, F., Coppola, L., Herrmann, M. J., Kessouri, F., and  
545 Estournel, C.: Budget of organic carbon in the North-Western Mediterranean open sea over the period 2004–  
546 2008 using 3-D coupled physical-biogeochemical modeling, *J. Geophys. Res. Ocean.*, 121, 7026–7055,  
547 <https://doi.org/10.1002/2016JC011818>, 2016.
- 548 Waldman, R., Herrmann, M., Somot, S., Arsouze, T., Benshila, R., Bosse, A., Chanut, J., Giordani, H., Sevault,  
549 F. and Testor, P.: Impact of the Mesoscale Dynamics on Ocean Deep Convection: The 2012–2013 Case Study  
550 in the Northwestern Mediterranean Sea, *J. Geophys. Res. Oceans.*,  
551 122, 8813–8840, doi:10.1002/2016JC01258, 2017b.
- 552 Waldman, R., Somot, S., Herrmann, M., Sevault, F., and Isachsen, P. E.: On the Chaotic Variability of Deep  
553 Convection in the Mediterranean Sea, *Geophys. Res. Lett.*, 45, 2433–2443,  
554 <https://doi.org/10.1002/2017GL076319>, 2018.
- 555 Waldman, R., Somot, S., Herrmann, M., Bosse, A., Caniaux, G., Estournel, C., Houpert, L., Prieur, L., Sevault,  
556 F., and Testor, P.: Modeling the intense 2012–2013 dense water formation event in the northwestern  
557 Mediterranean Sea: Evaluation with an ensemble simulation approach, *J. Geophys. Res.*  
558 *Oceans*, 122, 1297–1324, doi:10.1002/2016JC012437, 2017a.
- 559 Wang, B., LinHo, Zhang, Y., and Lu, M. M.: Definition of South China Sea monsoon onset and commencement  
560 of the East Asian summer monsoon, *J. Clim.*, 17, 699–710, <https://doi.org/10.1175/2932.1>, 2004.
- 561 Wang, Y., Fang, G., Wei, Z., Qiao, F., and Chen, H.: Interannual variation of the South China Sea circulation and



- 562 its relation to El Niño, as seen from a variable grid global ocean model, *J. Geophys. Res. Ocean.*, 111, 1–15,  
563 <https://doi.org/10.1029/2005JC003269>, 2006.
- 564 Wyrski, K.: Physical oceanography of the South East Asian Waters, *Naga Rep.*, 2, 1961.
- 565 Xie, S.-P., Xie, Q., and Wang, D.: Summer Upwelling in the South China Sea and its Role in Regional Climate  
566 Variations, *J. Geophys. Res.*, 108, 1–37, <https://doi.org/10.1029/2003JC001867>, 2003.
- 567 Xie, S. P., Chang, C. H., Xi, Q., and Wang, D.: Intraseasonal variability in the summer South China Sea: Wind  
568 jet, cold filament, and recirculations, *J. Geophys. Res. Ocean.*, 112, 1–11,  
569 <https://doi.org/10.1029/2007JC004238>, 2007.
- 570 Yu, Y., Wang, Y., Cao, L., Tang, R. and Chai, F.: The ocean-atmosphere interaction over a summer upwelling  
571 system in the South China Sea, *Journal of Marine Systems*, 208, 103360,  
572 <https://doi.org/10.1016/j.jmarsys.2020.103360>, 2020.
- 573 Zheng, Z. W., Zheng, Q., Kuo, Y. C., Gopalakrishnan, G., Lee, C. Y., Ho, C. R., Kuo, N. J., and Huang, S. J.:  
574 Impacts of coastal upwelling off east Vietnam on the regional winds system: An air-sea-land interaction, *Dyn.*  
575 *Atmos. Ocean.*, 76, 105–115, <https://doi.org/10.1016/j.dynatmoce.2016.10.002>, 2016.